

# Hydrophobic Polymer Encapsulation Effects on Subgap Density of States in Multilayered Molybdenum Disulfide Field-Effect Transistors

Sungju Choi, Seung Gi Seo, Hye Ri Yu, Seung Yeob Kim, Dae Hwan Kim,\* and Sung Hun Jin\*

Herein, exfoliated, multilayered molybdenum disulfide ( $\text{MoS}_2$ ) (m- $\text{MoS}_2$ ) field-effect transistors (FETs) are implemented with bilayered  $\text{SiN}_x/\text{SiO}_x$  gate dielectrics on indium tin oxide (ITO) substrates. For a quantitative understanding on gas adsorption effects on the electrical performance of m- $\text{MoS}_2$  FETs, subgap density of states (DOSs) in m- $\text{MoS}_2$  layers without (or with) hydrophobic polymer encapsulation are extracted using optical charge-pumping capacitance–voltage spectroscopy. Based on extracted subgap DOSs and their deconvolution with analytical model of acceptor (or donor) like states, all electrical parameters are systematically analyzed. More importantly, two times increase in field-effect mobility ( $\mu_{\text{FE}}$ ) is strongly related with decrease in shallow donor states ( $N_{\text{SD}}$ ) from  $2 \times 10^{18}$  to  $2 \times 10^{17} \text{ eV}^{-1} \text{ cm}^{-3}$ . In addition, significant improvement of sub-threshold swing (SS), hysteresis gap ( $V_{\text{HYS}}$ ) are attributed to the reduction of tail states ( $N_{\text{TA}}$ ) from  $4 \times 10^{19}$  to  $2 \times 10^{19} \text{ eV}^{-1} \text{ cm}^{-3}$ , along with decrease in midgap states ( $N_{\text{Mid}}$ ) from  $3 \times 10^{16}$  to  $1.3 \times 10^{16} \text{ eV}^{-1} \text{ cm}^{-3}$ . For a final validation, technology computer-aided design (TCAD) simulation with extracted DOS information nicely replicate measured  $I$ – $V$  characteristics for m- $\text{MoS}_2$  FETs without (or with) encapsulation, indicating that extracted DOS information is quite accurate, compared with implemented m- $\text{MoS}_2$  FETs.

electrons (e.g., suppression of source/drain direct tunneling leakage current in off regime), and 4) mechanical or/and chemical stability, and others.<sup>[2–8]</sup> Among various kinds of TMDCs, molybdenum disulfide ( $\text{MoS}_2$ ) has been predominately researched for the numerous applications such as transistors, memories, gas sensors, and photo-detectors due to their easy preparation via exfoliation (or chemical vapor deposition [CVD]), abundance of materials, decent stable properties, and others.<sup>[2,9]</sup> Regarding device applications based on  $\text{MoS}_2$ , electrical properties of single or multilayered  $\text{MoS}_2$  (m- $\text{MoS}_2$ ) field-effect transistors (FETs) are inevitably governed by defect states associated with several origins such as intrinsic defects of  $\text{MoS}_2$  layers, interface states between gate dielectrics and  $\text{MoS}_2$  layers, and gate dielectrics themselves.<sup>[10–14]</sup> Among the aforementioned origins, gas adsorption itself critically affects overall electrical performance of m- $\text{MoS}_2$  FETs due to large surface-to-volume ratio in 2D materials. Therefore, understanding


on gas adsorption effects is highly necessary to achieve the better electrical performance and the more reliable operation for m- $\text{MoS}_2$  FETs.

As the scaling-down of Si transistors less than 10 nm grows more tough due to physical limitation in the reduction of dimension around Si lattice constant ( $\approx 0.357 \text{ nm}$ ),<sup>[1]</sup> transition metal dichalcogenides (TMDCs) have been soared as one of viable options for the next-generation semiconductors because of several merits: 1) 2D nature of excellent electrostatic gate coupling, 2) negligible level of dangling bonds, 3) high-effective mass of

In this sense, external gas adsorption effects and their degradation on electrical properties of  $\text{MoS}_2$  FETs during direct current (DC) mode operation were studied in the different gas isolation environments via either vacuum pumping ( $\approx 10^{-6}$  Torr) or CYTOP passivation.<sup>[15–20]</sup> However, most of works for m- $\text{MoS}_2$  FETs have been done with gate dielectrics of thermal oxides on the top of heavily doped Si wafers as a common gate electrode structure. Thus, device performance for m- $\text{MoS}_2$  FETs with the most common gate dielectrics (e.g.,  $\text{SiO}_x$ ,  $\text{SiN}_x$ ) based on plasma-enhanced chemical vapor deposition (PECVD) are highly necessary to be investigated because m- $\text{MoS}_2$  FET backplanes for flat-panel displays (FPDs) can be one of promising future applications and their FET backplanes are typically implemented with PECVD  $\text{SiO}_x$  (or  $\text{SiN}_x$ ) dielectrics.<sup>[21]</sup> Moreover, device instability issues coming from  $\text{O}_2$  or  $\text{H}_2\text{O}$  absorption on the surface of  $\text{MoS}_2$  layers are ultimately necessary to be monitored and analyzed using the information on extracted density of states (DOSs) associated with either

S. Choi, H. R. Yu, Prof. D. H. Kim  
The School of Electrical Engineering  
Kookmin University  
Seoul 02703, South Korea  
E-mail: drlife@kookmin.ac.kr

S. G. Seo, S. Y. Kim, Prof. S. H. Jin  
Department of Electronic Engineering  
Incheon National University  
Academy-ro, Yeongsu-gu, Incheon 22012, South Korea  
E-mail: shjin@inu.ac.kr

 The ORCID identification number(s) for the author(s) of this article can be found under <https://doi.org/10.1002/pssr.201900492>.

DOI: 10.1002/pssr.201900492

exposed or suppressed external gas ambient. Interestingly, specific characterization of subgap DOSs for m-MoS<sub>2</sub> FETs associated with novel passivation methods are rarely reported up to now.<sup>[22,23]</sup>

More importantly, the accurate extraction of trap levels and their understanding on origin of traps are indispensable to achieving high performance of MoS<sub>2</sub> FETs. Thus, in a recent past, trap information on MoS<sub>2</sub> FETs has been quantitatively analyzed by several techniques, whereas the previous reports for characterization of subgap traps for m-MoS<sub>2</sub> FETs were limitedly addressed: 1)  $D_{it}$  characterization via Terman method,<sup>[24]</sup> 2) shallow traps nearby conduction band ( $E_c$ ) via multifrequency method,<sup>[22]</sup> and 3) deep-level traps through hysteretic gate transfer characteristics,<sup>[25]</sup> thereby entire characterization for subgap DOSs was fundamentally limited by method itself and its characterization. To compensate its limitation on method or validate its mechanism through another way, simulation-based approaches using DFT<sup>[23]</sup> and ab initio<sup>[26,27]</sup> are reported up to now. But, all entire characterization and its validation by using technology computer-aided design (TCAD) simulation for subgap DOS information on m-MoS<sub>2</sub> FETs before and after encapsulations are totally missing up to now.<sup>[26,27]</sup> Therefore, there is still much room for the improvement in the level of understanding on effects of subgap DOSs for m-MoS<sub>2</sub> FETs in this field. As one of fundamental and practical research activities, a systematic understanding on device performance of m-MoS<sub>2</sub> FETs with PECVD gate dielectrics either with or without novel passivation

is highly anticipated to enhance practical impacts in various applications toward backplanes of FPDs, flexible electronics, and Internet-of-Things sensors, etc.

In this study, we have implemented m-MoS<sub>2</sub> FETs with bilayered PECVD gate dielectrics (e.g., SiN<sub>x</sub>/SiO<sub>x</sub>) on indium tin oxide (ITO) glasses, followed by encapsulation of hydrophobic polymers of CYTOP, which have been validated for the passivation effects in previous literatures.<sup>[15,20,28]</sup> To identify the origin of device instability associated with external O<sub>2</sub> and H<sub>2</sub>O, to the best of our knowledge, this is the first report on quantitative trap characteristics, ranging from shallow traps (or donor-like traps) to deep-level traps (or acceptor-like traps), respectively, which have been analytically extracted using optical charge-pumping capacitance–voltage spectroscopy for m-MoS<sub>2</sub> FETs with PECVD dielectrics. With the well-established platform for CYTOP passivation, device performance with m-MoS<sub>2</sub> FETs with SiN<sub>x</sub>/SiO<sub>x</sub> dielectrics were isolated with external gas ambient and their effects on external gas adsorption in air were systematically analyzed by using the information of extracted subgap DOSs characterization without and with CYTOP encapsulation.

**Figure 1a** shows the process sequence for the fabrication of m-MoS<sub>2</sub> FETs. ITO glasses are used as a starting substrate. After cleaning ITO substrates, bilayered gate dielectrics (e.g., SiN<sub>x</sub>/SiO<sub>x</sub>) are deposited at the substrate temperature of 350 °C without vacuum breaking, followed by a gate contact opening, immediately m-MoS<sub>2</sub> exfoliation and transferred onto the SiN<sub>x</sub>/SiO<sub>x</sub> dielectrics. After inspection of m-MoS<sub>2</sub> flakes and their

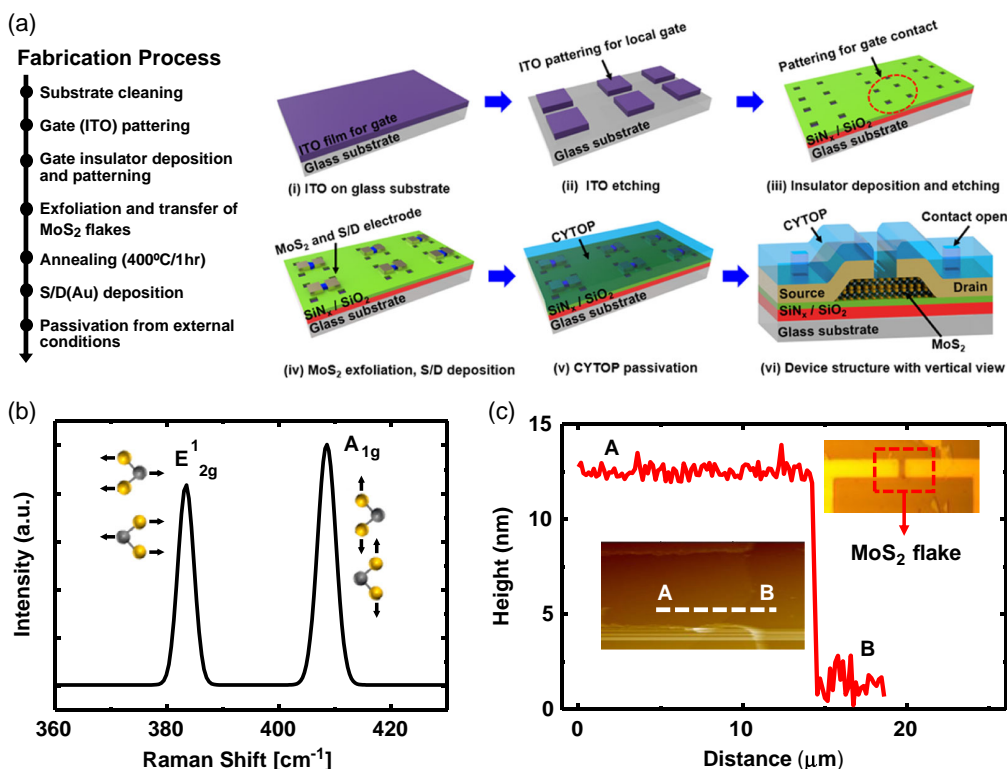


**Figure 1.** a) Schematic cartoons for process flows to implement CYTOP-passivated m-MoS<sub>2</sub> FETs. b) Raman spectra of the m-MoS<sub>2</sub>. Insets describe the two characteristic vibrational modes of MoS<sub>2</sub>, in-plane vibration mode E<sub>2g</sub><sup>1</sup> and out-of-plane vibration mode A<sub>1g</sub>. c) Surface profiles, along with white dashed lines, are scanned by AFM. Insets in (c) show optical microscope images for m-MoS<sub>2</sub> FETs. A and B in the inset denote the location of MoS<sub>2</sub> and oxide (SiO<sub>2</sub>), respectively. The channel width-to-length ratio (W/L) is 30/10 μm for m-MoS<sub>2</sub> FETs.

annealing in Ar/H<sub>2</sub> ambient, source/drain electrodes were formed on m-MoS<sub>2</sub> layers via thermal evaporation of Au, yielding m-MoS<sub>2</sub> FETs. Figure 1b shows Raman spectroscopy for m-MoS<sub>2</sub> layers (peak difference ≈25 cm<sup>-1</sup>), identifying that m-MoS<sub>2</sub> were used as active layers in the channel. Thereafter, atomic force microscopy (AFM) analysis, as shown in Figure 1c, confirmed that thickness of m-MoS<sub>2</sub> is 12.5 nm which is equivalently extracted as 19 layers of MoS<sub>2</sub> in the channel regime. For the evaluation on external gas ambient effects on the performance of m-MoS<sub>2</sub> FETs, electrical characteristics before encapsulation of CYTOP were evaluated with the same protocols reported in literature.<sup>[15]</sup> For a fair comparison study, all electrical characteristics without and with CYTOP encapsulation were evaluated and systematic comparison was performed.

Figure 2a shows representative transfer characteristics for m-MoS<sub>2</sub> FETs with and without CYTOP encapsulation among 14 devices (see Figure S1, Supporting Information). All electrical parameters such as threshold voltage ( $V_{TH}$ ), hysteresis gap ( $V_{HYS}$ ), subthreshold swing (SS), and field-effect mobility ( $\mu_{FE}$ ) are systematically extracted and statistically analyzed. SS was extracted with relation of  $SS = [|\partial \log I_{DS} / \partial V_{GS}|_{max}]^{-1}$ .  $\mu_{FE}$  is defined as  $g_m / (C_{GI} \cdot W/L \cdot V_{DS})$  where  $g_m$  is transconductance and  $C_{GI}$  is gate dielectric capacitance per area. In addition,  $V_{HYS}$  was extracted as the difference in  $V_{TH}$  between forward-swept and reverse-swept transfer characteristics, respectively. All electrical parameters for 14 devices are extracted and analyzed in a statistical mode (see Figure S2 and S3, Supporting

Information). In addition, Figure 2b shows that output characteristics, at a low drain bias condition less than 1 V range, is linear, indicating that m-MoS<sub>2</sub> FETs have good ohmic contact properties. Regardless of CYTOP passivation, output curves for m-MoS<sub>2</sub> FETs with 10  $\mu$ m channel length show decent saturation behaviors as drain bias increases. After CYTOP encapsulation,  $V_{HYS}$  reduction and its on-current enhancement were consistently and reproducibly observed (see Figure S1, Supporting Information). For the statistical analysis on  $V_{HYS}$  and SS for m-MoS<sub>2</sub> FETs with and without CYTOP encapsulation, raw data on  $V_{HYS}$  and SS were analytically fitted with the normal probability density function (n-PDF) according to the equation:  $f(x) = \frac{1}{\sqrt{2\pi}\sigma} \exp\left(-\frac{(x-m)^2}{2\sigma^2}\right)$ , where  $\sigma$  and  $m$  are standard deviation and mean, respectively (see Figure S2 and S3, Supporting Information). Figure 2c shows significant reduction of an average value ( $m$ ) of  $V_{HYS}$  from 1.94 to 1.20 V, denoting that a standard deviation ( $\sigma$ ) was noticeably reduced from 1.47 to 0.47 V. Moreover, Figure 2d shows SS distribution for m-MoS<sub>2</sub> FETs with and without CYTOP passivation, indicating that reduction of SS and variation is also reduced significantly. Apparent CYTOP passivation effects on  $V_{HYS}$  and SS were reproducibly observed. However, fundamental origins of performance improvement and their correlation with subgap DOSs are ultimately necessary for understanding of device design rule for the better performance of m-MoS<sub>2</sub> FETs.

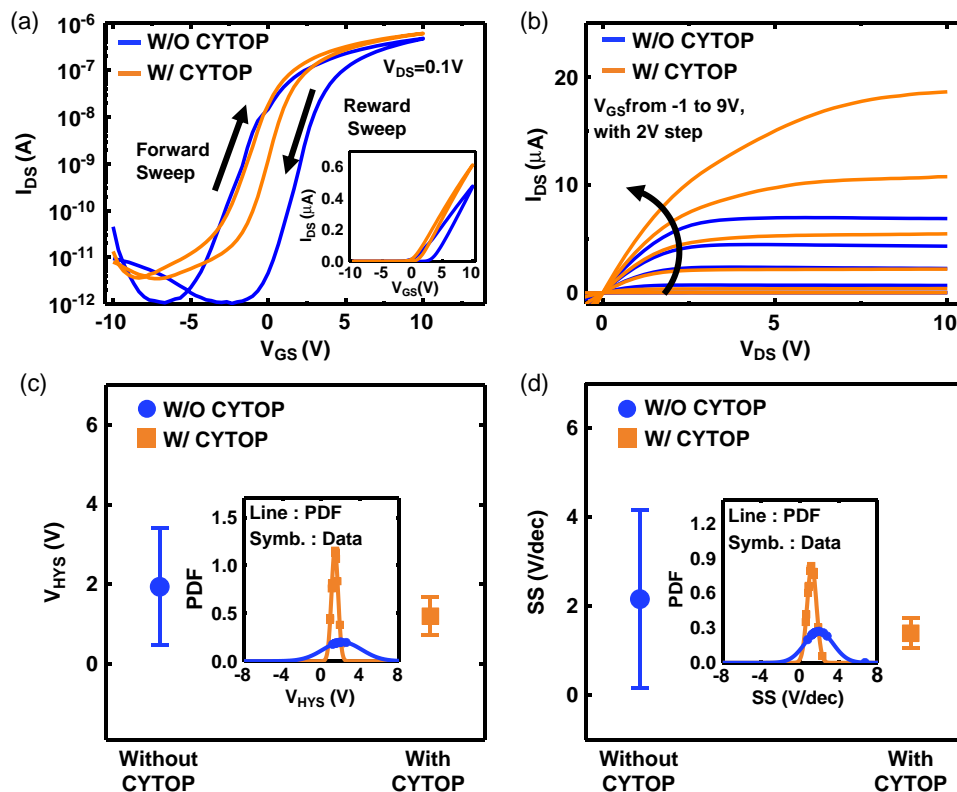


**Figure 2.** a) Transfer characteristics of m-MoS<sub>2</sub> FETs before and after CYTOP passivation at  $V_{DS} = 0.1$  V in log scale. Inset figures show transfer characteristics in linear scale. b) Output characteristics of m-MoS<sub>2</sub> FETs with  $V_{GS}$  from 0 to  $-3$  V (0.5 V step). Distributions of c) hysteresis gap ( $V_{HYS}$ ) and d) SS for m-MoS<sub>2</sub> FETs without and with CYTOP passivation.

Thus, we utilized a well-established optical charge-pumping  $C$ - $V$  spectroscopy for the extraction of subgap DOSs in m-MoS<sub>2</sub> FETs.<sup>[29–31]</sup> The technique, as shown in **Figure 3a**, is basically using monochromatic photonic capacitance–voltage ( $C$ - $V$ ) (MPCV) characterization (see Figure S4, Supporting Information). With the solid platforms, previously reported in literatures<sup>[29–31]</sup> for the extraction of subgap DOSs, the capacitance between bottom gate and source/drain electrodes for m-MoS<sub>2</sub> FETs was evaluated, respectively, in dark and light with a laser wavelength ( $\lambda$ ) of 1065 nm.  $C$ - $V$  characteristics were measured by the HP4284A precision LCR meter at the frequency of 10 kHz in dark and light with a wavelength of  $\lambda = 1065$  nm to extract full range of trap information in sub-band gaps. Figure 3a shows a schematic cartoon and an equivalent circuit for m-MoS<sub>2</sub> FETs with bottom gate configuration. In general, minimum of capacitance ( $C_{\min}$ ) is determined by total overlapped areas between the source and drain electrodes ( $C_{\text{PAD,S}}$  and  $C_{\text{PAD,D}}$ ) and the gate electrodes. In addition, the capacitance difference ( $C_{\max} - C_{\min}$ ) between maximum of capacitance ( $C_{\max}$ ) and minimum of capacitance ( $C_{\min}$ ) leads to MoS<sub>2</sub> layer capacitance ( $C_{\text{MoS}_2}$ ) which can be modulated by  $V_{\text{GS}}$ , as shown Figure 3a. Figure 3b,c shows the photonic  $C$ - $V$  for m-MoS<sub>2</sub> FETs with CYTOP and without CYTOP, respectively. Different response behaviors under the same condition for light excitation are shown in Figure 3b,c.

With the established platforms and their extraction procedures reported in the literatures,<sup>[30,31]</sup> **Figure 4a** shows that subgap DOSs for m-MoS<sub>2</sub> FETs with and without CYTOP are extracted from measured photonic  $C$ - $V$  as shown in Figure 3b,c. Subgap DOSs are analytically modeled and deconvoluted by acceptor-like states (DOSs) and donor-like states (DOSs) according to Equation (1) and (2)

$$g_{\text{TA}}(E) + g_{\text{DA}}(E) = N_{\text{TA}} \exp\left(-\frac{E_{\text{C}} - E}{kT_{\text{TA}}}\right) + N_{\text{DA}} \exp\left(-\frac{E_{\text{C}} - E}{kT_{\text{DA}}}\right) \quad (1)$$

$$g_{\text{TD}}(E) + g_{\text{SD}}(E) + g_{\text{Mid}}(E) = N_{\text{TD}} \exp\left(-\frac{E - E_{\text{V}}}{kT_{\text{TD}}}\right) + N_{\text{SD}} \exp\left(-\left(\frac{E_{\text{C}} - E_{\text{SD}} - E}{kT_{\text{SD}}}\right)^2\right) + N_{\text{Mid}} \exp\left(-\left(\frac{E - E_{\text{V}} - E_{\text{Mid}}}{kT_{\text{Mid}}}\right)^2\right) \quad (2)$$

where  $g_{\text{TA}}(E)$  is for acceptor-like tail state,  $g_{\text{DA}}(E)$  for acceptor-like deep state,  $g_{\text{TD}}(E)$  for donor-like tail states,  $g_{\text{SD}}(E)$  for shallow-donor states, and  $g_{\text{Mid}}(E)$  for midgap defect state, depending on the type of energy-level distribution. In addition, each characteristic energy distribution and Gaussian center of energy are defined as  $kT_{\text{DOS}}$  (e.g.,  $T_{\text{TA}}$ ,  $T_{\text{DA}}$ ,  $T_{\text{TD}}$ ,  $T_{\text{SD}}$ , and  $T_{\text{Mid}}$ ) and  $E_{\text{DOS}}$  (e.g.,  $E_{\text{SD}}$  and  $E_{\text{Mid}}$ ), respectively. Herein, each energy density distribution is defined as  $N_{\text{DOS}}$  (e.g.,  $N_{\text{TA}}$ ,  $N_{\text{DA}}$ ,  $N_{\text{TD}}$ ,  $N_{\text{SD}}$ , and  $N_{\text{Mid}}$ ),  $E_{\text{V}}$  for the valance band maximum, and  $E_{\text{C}}$  for the conduction band minimum which are well fitted with the model parameters shown by Equation (1) and (2).

All extracted subgap DOSs are fitted with the analytical models based on Equation (1) and (2), leading to smooth functions for subgap DOSs as shown in Figure 4b. Noticeable changes in DOSs are observed and compared, as shown in Figure 4b. For the quantitative understanding, subgap DOSs are deconvoluted using conventional trap states such as acceptor-like (e.g., Equation (1)) and donor-like states (e.g., Equation (2)), respectively. Generally, in semiconductors, donor-like defect states are charge-neutral when occupied by electrons and positively charged when empty, whereas acceptor-like states are

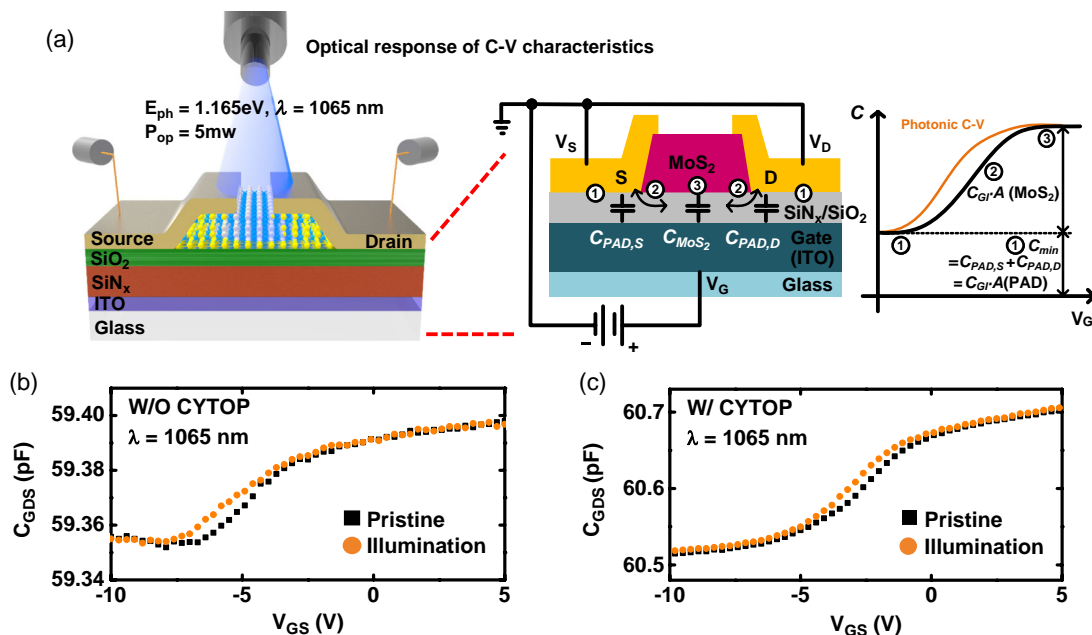


**Figure 3.** a) Schematic cartoons of optical charge-pumping method for DOS characterization including device structure and conceptual schematic for extracting capacitance value. Measured capacitance data in dark and near-infrared range illumination (wavelength = 1065 nm) for m-MoS<sub>2</sub> FETs: b) without and c) with CYTOP passivation.

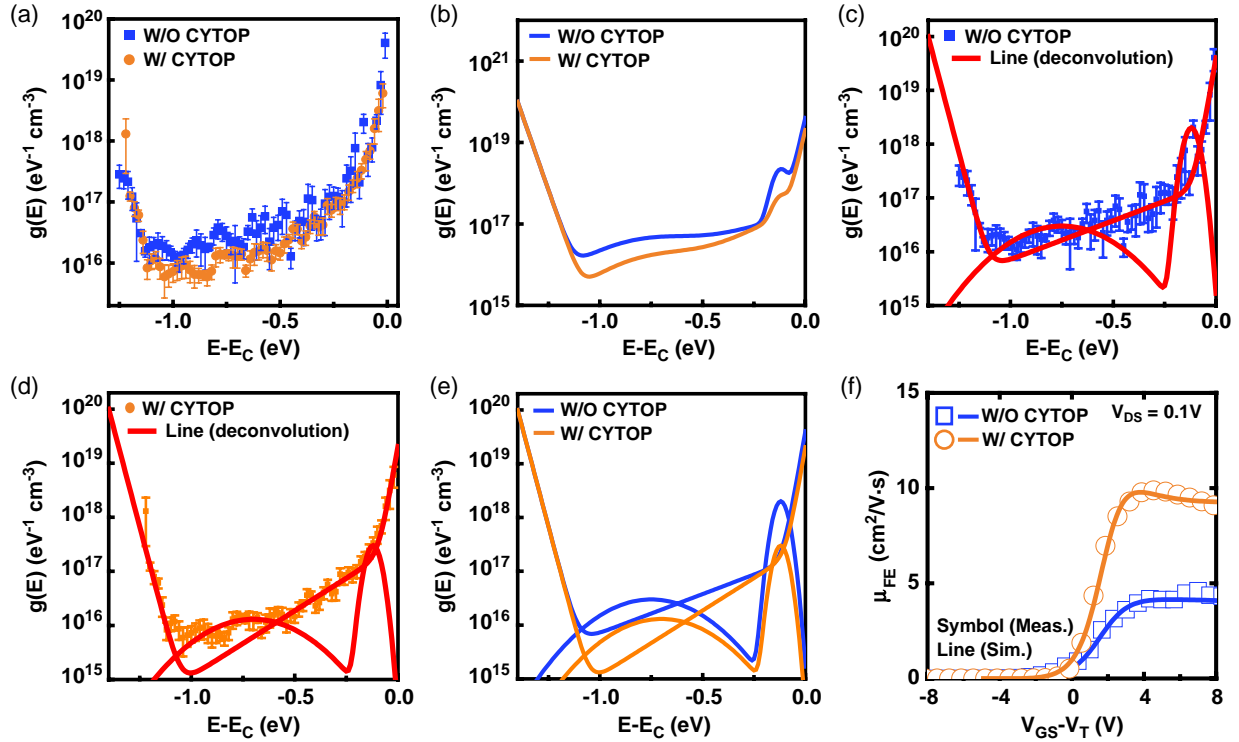


**Figure 4.** a) Subgap DOSs extracted from m-MoS<sub>2</sub> FETs with and without passivation. b) Overlapped extracted subgap DOSs fitted with TCAD model. Measured (symbols) and deconvoluted (lines) DOSs ( $g(E)$ ) for m-MoS<sub>2</sub> FETs: c) without and d) with CYTOP, respectively. e) Overlapped deconvoluted subgap DOS ( $g(E)$ ) for m-MoS<sub>2</sub> FETs with and without CYTOP, for the better comparison. f) Measured (symbols) and TCAD model-based (lines) field-effect mobility ( $\mu_{FE}$ ) for m-MoS<sub>2</sub> FETs with respect to a gate-over drive ( $= V_{GS}-V_{TH}$ ). Squares and circles denote m-MoS<sub>2</sub> FETs with and without CYTOP passivation, respectively.

charge-neutral when empty and negatively charged when occupied by electrons. Figure 4c shows deconvoluted model curves for subgap DOSs, which are fitted with experimentally extracted DOS for m-MoS<sub>2</sub> FETs without CYTOP encapsulation. Also, Figure 4d shows the deconvoluted model curves which are fitted with data for m-MoS<sub>2</sub> FETs with CYTOP encapsulation. For the representation of discernable difference in two states of DOSs, Figure 4e shows comparison of subgap DOS graphs for m-MoS<sub>2</sub> FETs with and without CYTOP passivation, respectively.

Thereafter, subgap DOS parameters are systematically modeled and extracted. All extracted parameters in a concise mode

are shown in **Table 1**. Overall,  $N_{TA}$  level was at least two times reduced from  $4 \times 10^{19}$  to  $2 \times 10^{19} \text{ eV}^{-1} \text{ cm}^{-3}$ , whereas acceptor-like Gaussian states ( $N_{DA}$ ) are extracted as the same level of  $2 \times 10^{17} \text{ eV}^{-1} \text{ cm}^{-3}$ . In addition, after consideration of physical thickness of m-MoS<sub>2</sub> layers, areal density of  $N_{TA}$  was extracted in the range from  $6 \times 10^{13}$  to  $3 \times 10^{13} \text{ eV}^{-1} \text{ cm}^{-2}$  in Figure S5, Supporting Information, and compared with the value without consideration of the thickness of m-MoS<sub>2</sub> layers. Overall, extracted values in this study are one order of magnitude higher than that of m-MoS<sub>2</sub> FETs with thermal oxide with Al<sub>2</sub>O<sub>3</sub> encapsulation, extracted using multifrequency method.<sup>[22]</sup> This is

**Table 1.** Summary of model parameters which are extracted from acceptor-like and donor-like state models to be fitted with subgap DOSs ( $g(E)$ ) for m-MoS<sub>2</sub> FETs with and without CYTOP passivation, respectively.

	Without CYTOP	With CYTOP
Acceptor-like states (DOSs)	$g_{TA}(E) + g_{DA}(E) = N_{TA} \times \exp\left(-\frac{E_c - E}{kT_{TA}}\right) + N_{DA} \times \exp\left(-\frac{E_c - E}{kT_{DA}}\right)$	
$N_{TA} (\text{eV}^{-1} \text{ cm}^{-3})/kT_{TA} (\text{eV})$	$4 \times 10^{19}/0.02$	$2 \times 10^{19}/0.02$
$N_{DA} (\text{eV}^{-1} \text{ cm}^{-3})/kT_{DA} (\text{eV})$	$2 \times 10^{17}/0.3$	$2 \times 10^{17}/0.2$
Donor-like states (DOSs)	$g_{TD}(E) + g_{SD}(E) + g_{Mid}(E) = N_{TD} \times \exp\left(-\frac{E - E_V}{kT_{TD}}\right) + N_{SD} \times \exp\left(-\left(\frac{E_c - E_{SD} - E}{kT_{SD}}\right)^2\right) + N_{Mid} \times \exp\left(-\left(\frac{E - E_V - E_{Mid}}{kT_{Mid}}\right)^2\right)$	
$N_{TD} (\text{eV}^{-1} \text{ cm}^{-3})/kT_{TD} (\text{eV})$	$1 \times 10^{20}/0.03$	
$N_{SD} (\text{eV}^{-1} \text{ cm}^{-3})/kT_{SD} (\text{eV})/E_{SD} (\text{eV})$	$2 \times 10^{18}/0.045/0.2$	$2 \times 10^{17}/0.045/0.2$
$N_{Mid} (\text{eV}^{-1} \text{ cm}^{-3})/kT_{Mid} (\text{eV})/E_{Mid} (\text{eV})$	$3 \times 10^{16}/0.3/0.7$	$1.3 \times 10^{16}/0.3/0.7$

possibly due to more rough surface of PECVD gate dielectrics as compared with thermal oxide, and encapsulation method change from the inorganic  $\text{Al}_2\text{O}_3$  to polymer CYTOP encapsulation. However, characteristic energy distribution for Gaussian states ( $kT_{\text{DA}}$ ) was reduced from 0.3 to 0.2 eV, indicating that trap distribution was narrowed down, possibly due to the prevention of adsorption of  $\text{O}_2$  and moisture (e.g.,  $\text{H}_2\text{O}$  or  $\text{OH}^-$ ) on the surface of m-MoS<sub>2</sub> active layers in air with the help of CYTOP passivation. This result also substantiates the fact that the reduction of hysteresis gap after CYTOP passivation, as shown in Figure 2c, is possibly related with  $kT_{\text{DA}}$  reduction. Moreover, the hysteresis effect is known to change  $V_{\text{TH}}$  when sweeping the transfer curve from negative  $V_{\text{GS}}$  to positive  $V_{\text{GS}}$  and then sweeping the transfer curve from positive to negative bias of  $V_{\text{GS}}$  again, which affects setting time of circuit and switching speed.<sup>[32]</sup> That is, after accumulated carriers are trapped in shallow or deep traps, the nonemitted carriers will cause a screen effect on the gate bias. One of origins for hysteresis gap is mainly due to  $\text{O}_2$  or  $\text{OH}^-$  in air during the sweep, which changes the  $V_{\text{TH}}$  by being adsorbed onto the surface of m-MoS<sub>2</sub>.<sup>[18,19]</sup> After passivation, the hysteresis gap is noticeably decreased due to the reduction of total trap sites of m-MoS<sub>2</sub>, possibly coming from  $\text{OH}^-$  groups attached to m-MoS<sub>2</sub>. In particular, extracted values of  $N_{\text{TA}}$  ( $\approx 6 \times 10^{13} \text{ eV}^{-1} \text{ cm}^{-2}$ ) in this work are within the value of  $D_{\text{it}}$  extracted by Terman method for m-MoS<sub>2</sub> layers,<sup>[24]</sup> which are mainly ascribed to sulfur vacancy in m-MoS<sub>2</sub> layers with the energy location of 0.3–0.47 eV above from midgap energy level in energy bandgap ( $E_{\text{g}}$ ) regardless of gate dielectrics.

In contrast, the number of tail states ( $N_{\text{TD}}$ ) and energy characteristics ( $kT_{\text{D}}$ ) for donor-like states (DOSs) are extracted as the same level of  $1 \times 10^{20} \text{ eV}^{-1} \text{ cm}^{-3}$  and 0.03 eV, respectively. Moreover,  $N_{\text{SD}}$  level was noticeably reduced from  $2 \times 10^{18}$  to  $2 \times 10^{17} \text{ eV}^{-1} \text{ cm}^{-3}$ , within the negligible change from the value of  $kT_{\text{SD}}$  ( $\approx 0.045 \text{ eV}$ ) and  $E_{\text{SD}}$  ( $\approx 0.2 \text{ eV}$ ). One-decade reduction for  $N_{\text{SD}}$  was noticeably observed, which is a good indication why on-current for m-MoS<sub>2</sub> FETs is significantly improved after CYTOP passivation. This is strongly related with the reduction of events for the impurity scattering during free carrier transport in the m-MoS<sub>2</sub> channel, leading to a field-effect mobility enhancement after CYTOP passivation. More importantly, decrease in midgap states ( $N_{\text{Mid}}$ ) from  $3 \times 10^{16}$  to  $1.3 \times 10^{16} \text{ eV}^{-1} \text{ cm}^{-3}$  was also observed, hinting that possible passivation of sulfur vacancy could be involved in the hysteresis gap reduction because CYTOP was passivated on the back channel of m-MoS<sub>2</sub> FETs. Moreover, the reduction of  $N_{\text{Mid}}$  and  $N_{\text{SD}}$  after CYTOP encapsulation is well matched with the previous reports on sulfur vacancy encapsulation, investigated by DFT simulation for the effects of encapsulation.<sup>[23]</sup> Herein, field-effect mobility ( $\mu_{\text{FE}}$ ) and electron concentration ( $n_{\text{e}}$ ) determine electrical conductivity according to the relationship of  $\sigma = n_{\text{e}} e \mu_{\text{FE}}$ . Actually, the effect of  $E_{\text{f}}$  lowering associated with  $N_{\text{sd}}$  reduction is negligible due to the logarithmic relationship ( $E_{\text{c}} - E_{\text{f}} = kT \ln(N_{\text{c}}/n_{\text{o}})$ ). Consequently,  $N_{\text{Mid}}$  and  $N_{\text{sd}}$  reduction can significantly contribute to the increase in field-effect mobility ( $\mu_{\text{FE}}$ ), leading to prominent observation of current level increase in transfer characteristics. In addition, hysteresis gap ( $V_{\text{HYS}}$ ) and SS variation were apparently reduced right after CYTOP passivation. This is attributed to the decrease in trap levels in subgap states, leading to noticeable reduction of

variation in terms of frequency of events both variable range hopping (VRH) and multiple trapping and release (MTR).

One of the strong and reproducible observations is the enhancement of on-current after CYTOP passivation. This is strongly attributed to the enhancement of field-effect mobility, thereby direct comparison in extracted field-effect mobility is given in the same graph as shown in Figure 4e. It is typically reported that the electrical performance in n-channel FETs is significantly affected by the states near  $E_{\text{c}}$ .<sup>[33,34]</sup> Several key parameters such as  $g_{\text{TA}}(E)$ ,  $g_{\text{SD}}(E)$ , and  $g_{\text{DA}}(E)$  around  $E_{\text{c}}$  are both energetically distributed throughout the energy bandgap with energy location dependency, yielding capture and thermal release of free carriers in certain energy states (i.e., multiple trapping and thermal release events).<sup>[35]</sup> Thus, this effect decreases a mean free path of free carriers, leading to degradation of field-effect mobility in free carriers (see Figure S6 and S7, Supporting Information). All these mechanisms are well matched with all the observed improvement of field-effect mobility after CYTOP passivation.

Overall, all extracted values in Table 1 show the reduction of  $g_{\text{TA}}(E)$ ,  $g_{\text{SD}}(E)$ , and  $g_{\text{DA}}(E)$  near the  $E_{\text{c}}$  after passivation. This reduced the number of trap density that needs to be filled and the capture probability from free carriers on the  $E_{\text{c}}$  to trap sites was reduced after passivation. Reduced trap sites improve the electrical parameters such as mobility and SS.<sup>[33–36]</sup> This is coming from passivation effects to prohibit  $\text{O}_2$  and  $\text{H}_2\text{O}$  from being adsorbed on the surface of m-MoS<sub>2</sub>, strongly associated with passivation and reduction effects with  $\text{H}_2\text{O}$  and sulfur vacancy or/and Mo 4s orbital disorder.

To validate extracted subgap DOSs from the perspective of device operation, a TCAD simulation was conducted using Atlas 2D of Silvaco. Figure 5a,b shows that simulated  $I$ – $V$  characteristics (see Figure S8, Supporting Information) are immediately compared with  $I$ – $V$  characteristics in DC mode, which were measured at room temperature under dark ambient using an Agilent 4156C precision semiconductor parameter analyzer. The transfer characteristics were measured at a fixed drain-to-source voltage ( $V_{\text{DS}}$ ) of 0.1 V and output characteristics were evaluated. With the condition of extracted field-effect mobility as one of input parameters, transfer and output characteristics in TCAD simulation are self-validated with the same measured transfer characteristics, substantiating that extracted subgap DOS information is valid in  $I$ – $V$  characteristics.

In this study, quantitative analysis on subgap states for m-MoS<sub>2</sub> FETs before and after CYTOP encapsulation were performed using optical charge-pumping capacitance–voltage spectroscopy. Hysteresis gap reduction and field-effect mobility improvement are strongly involved in  $N_{\text{TA}}$ ,  $N_{\text{SD}}$  reduction after CYTOP passivation, which are well matched with statistically extracted subgap DOS information. In addition, to the best of our knowledge, PECVD  $\text{SiN}_x/\text{SiO}_x$  are applied for gate dielectrics toward m-MoS<sub>2</sub> FETs, and their CYOTP passivation effects are quantitatively analyzed for the first time via subgap DOS extraction and their systematic comparison. All extracted subgap DOSs in this work are well matched with previously reported trap levels which were investigated with different techniques (e.g., Terman method, multifrequency method, and hysteretic gate transfer characteristic-based extractions). More importantly, TCAD simulation itself is self-validated between extracted- and

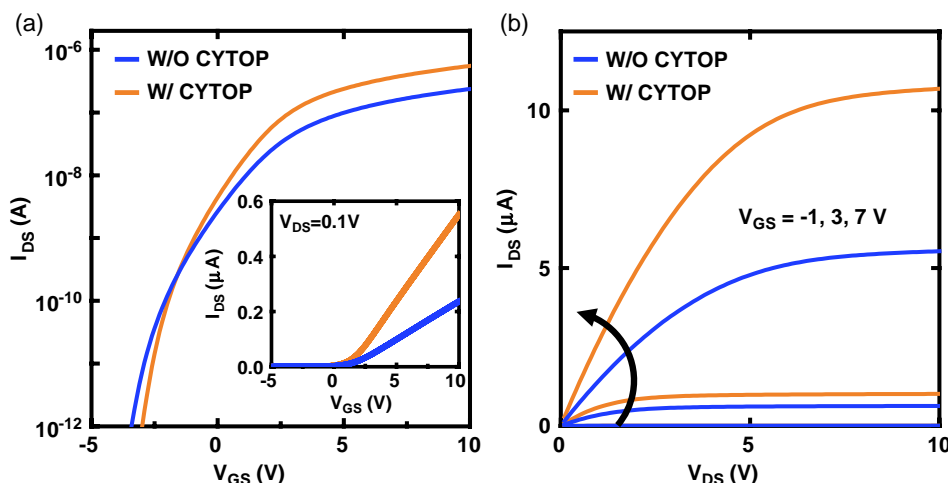


**Figure 5.** Validation on transfer and output characteristics for m-MoS<sub>2</sub> FETs: TCAD simulated a) transfer characteristics and b) output characteristics for m-MoS<sub>2</sub> FETs with and without CYTOP passivation, respectively. Inset in (a) shows transfer characteristics in a linear scale.

simulation-based subgap DOS information, substantiating that CYTOP passivation and their mechanisms over performance improvement are closely related with acceptor-like tail states and deep-level traps in the entire range of energy bandgap of m-MoS<sub>2</sub>.

## Experimental Section

**FET Fabrication and Characterization:** An ITO-coated glass was used as a starting substrate, playing the role of gate electrode, followed by ITO etching by dipping in ITO etchant solution to make island structure. After etching, gate insulator layer of SiN<sub>x</sub>/SiO<sub>2</sub> (200 nm/50 nm) was deposited by PECVD. Thereafter, multilayers of MoS<sub>2</sub> were mechanically exfoliated from bulk MoS<sub>2</sub> crystals (SPI Supplies, 429ML-AB) and transferred onto ITO glass substrates using poly dimethylsiloxane (PDMS) elastomer. Immediate annealing was performed in a mixed gas (≈Ar/H<sub>2</sub>) at the temperature of 400 °C during 1 h, to remove organic residues on the MoS<sub>2</sub> flakes which might contaminate them during the transfer process. Thereafter, a 30-nm-thick layer of Au was evaporated using thermal evaporators, followed by lifting off on a photo lithographically patterned area, forming the source/drain electrodes. All the electrical characterizations were measured with a semiconductor parameter Analyzer (Agilent 4156C) in ambient air. Transfer characteristics were obtained at V<sub>DS</sub> = 0.1 V. The thickness of MoS<sub>2</sub> flakes was measured by the AFM (Park system, XE-100). Raman spectrometer (WITEC alpha300) was used to analyze the Raman spectra of MoS<sub>2</sub> flakes with a 532 nm laser excitation.

**Optical Charge-Pumping Capacitance–Voltage Spectroscopy:** All the electrical characterizations were measured with a semiconductor impedance analyzer (Agilent 4284 A) in ambient air at room temperature. Then, C–V measurements were conducted at 100 kHz from V<sub>GS</sub> = –10 to V<sub>GS</sub> = 5 V, with one terminal connected to the gate, whereas the other terminal connected to the source and drain electrically tied together. Then, C–V measurements were obtained in dark and monochromatic illumination at a wavelength of 1065 nm.

**TCAD Validation:** TCAD simulations were performed by incorporating the band structure, subgap DOS model, advance mobility, and tunneling model into Silvaco ATLAS-2D. The band structure was simplified to several quantities: the energies of the conduction and valence band edges and the DOSs masses for electrons and holes of each material. Trap-limited transport model was all activated in this simulation. In addition, an advance

mobility model that includes phonon scattering, Coulomb scattering, surface roughness, and subgap DOS effects was applied.

## Supporting Information

Supporting Information is available from the Wiley Online Library or from the author.

## Acknowledgements

S.C. and S.G.S. contributed equally to this work. This work was supported by National Research Foundation of Korea (NRF) funded by the Ministry of Science, ICT & Future Planning (NRF-2017R1A2B2009042) and in part by the National Research Foundation of Korea (NRF) through the Korean Government, Ministry of Education, Science and Technology (MEST) (grant numbers 2016R1A5A1012966 and 2017R1A2B4006982).

## Conflict of Interest

The authors declare no conflict of interest.

## Keywords

encapsulation, density of states, field-effect transistors, molybdenum disulfide, technology computer-aided design simulations

Received: September 1, 2019

Revised: November 14, 2019

Published online:

- [1] T. Hom, W. Kiszenick, B. Pos, *J. Appl. Crystallogr.* **1975**, *8*, 457.
- [2] X. Huang, Z. Zeng, H. Zhang, *Chem. Soc. Rev.* **2013**, *42*, 1934.
- [3] M. Chhowalla, H. S. Shin, G. Eda, L.-J. Li, K. P. Loh, H. Zhang, *Nat. Chem.* **2013**, *5*, 263.
- [4] B. Radisavljevic, A. Radenovic, J. Brivio, V. Giacometti, A. Kis, *Nature Nanotechnol.* **2011**, *6*, 147.

- [5] K. K. H. Smithe, C. D. English, S. V. Suryavanshi, E. Pop, *Nano Lett.* **2018**, *18*, 4516.
- [6] R. Fivaz, E. Mooser, *Phys. Rev.* **1967**, *163*, 743.
- [7] Y. Huang, L. Zhu, Q. Zhao, Y. Guo, Z. Ren, J. Bai, X. Xu, *ACS Appl. Mater. Interfaces* **2017**, *9*, 4956.
- [8] R. Soref, B. Bennett, *IEEE J. Quantum Electron.* **1987**, *23*, 123.
- [9] D. Jariwala, V. K. Sangwan, L. J. Lauhon, T. J. Marks, M. C. Hersam, *ACS Nano* **2014**, *8*, 1102.
- [10] N. Liu, J. Baek, S. M. Kim, S. Hong, Y. K. Hong, Y. S. Kim, H.-S. Kim, S. Kim, J. Park, *ACS Appl. Mater. Interfaces* **2017**, *9*, 42943.
- [11] C. Lee, S. Rathi, M. A. Khan, D. Lim, Y. Kim, S. J. Yun, D.-H. Youn, K. Watanabe, T. Taniguchi, G.-H. Kim, *Nanotechnology* **2018**, *29*, 335202.
- [12] J. Shu, G. Wu, Y. Guo, B. Liu, X. Weia, Q. Chen, *Nanoscale* **2016**, *8*, 3049.
- [13] X. Zou, J. Xu, H. Huang, Z. Zhu, H. Wang, B. Li, L. Liao, G. Fang, *Nanotechnology* **2018**, *29*, 245201.
- [14] Y. Guo, X. Wei, J. Shu, B. Liu, J. Yin, C. Guan, Y. Han, S. Gao, Q. Chen, *Appl. Phys. Lett.* **2015**, *106*, 103109.
- [15] J. K. Roh, I. T. Cho, H. W. Shin, G. W. Baek, B. H. Hong, J. H. Lee, S. H. Jin, C. H. Lee, *Nanotechnology* **2015**, *26*, 455201.
- [16] H. Qiu, L. Pan, Z. Yao, J. Li, Y. Shi, X. Wang, *Appl. Phys. Lett.* **2012**, *100*, 123104.
- [17] H.-J. Kwon, J. Jang, S. Kim, V. Subramanian, C. P. Grigoropoulos, *Appl. Phys. Lett.* **2014**, *105*, 152105.
- [18] K. Cho, W. Park, J. Park, H. Jeong, J. Jang, T.-Y. Kim, W.-K. Hong, S. Hong, T. Lee, *ACS Nano* **2013**, *7*, 7751.
- [19] D. J. Late, B. Liu, H. S. S. R. Matte, V. P. Dravid, C. N. R. Rao, *ACS Nano* **2012**, *6*, 5635.
- [20] S. G. Seo, S. H. Jin, *IEEE Trans. Electron Devices* **2019**, *66*, 2208.
- [21] C.-H. Lee, N. Vardy, W. S. Wong, *IEEE Trans. Electron Devices* **2016**, *37*, 731.
- [22] H. Bae, C. K. Kim, Y. K. Choi, *AIP Adv.* **2017**, *7*, 075304.
- [23] H. Lu, A. Kummel, J. Robertson, *Appl. Phys. Lett.* **2018**, *6*, 066104.
- [24] M. Takenaka, Y. Ozawa, J. Han, S. Takagi, in *2016 IEEE Int. Electron Devices Meet.*, IEEE, San Francisco, CA **2016**, pp. 5.8.1–5.8.4.
- [25] Q. Xu, Y. Sun, P. Yang, Y. Dan, *AIP Adv.* **2019**, *9*, 015230.
- [26] L. Li, R. Long, T. Bertolini, O. V. Prezhdo, *Nano Lett.* **2017**, *17*, 7962.
- [27] E. Ponomarev, Á. Pásztor, A. Waelchli, A. Scarfato, N. Ubrig, C. Renner, *ACS Nano* **2018**, *12*, 2669.
- [28] S. G. Seo, J. H. Hong, J. H. Ryu, S. H. Jin, *IEEE Trans. Electron Devices* **2019**, *40*, 251.
- [29] K. Jeon, C. Kim, I. Song, J. Park, S. Kim, S. Kim, Y. Park, J.-H. Park, S. Lee, D. M. Kim, D. H. Kim, *Appl. Phys. Lett.* **2008**, *93*, 182102.
- [30] J.-H. Park, K. Jeon, S. Lee, S. Kim, S. Kim, I. Song, C. J. Kim, J. Park, Y. Park, D. M. Kim, D. H. Kim, *IEEE Electron Device Lett.* **2008**, *29*, 1292.
- [31] H. Bae, H. Choi, S. Jun, C. Jo, Y. H. Kim, J. S. Hwang, J. Ahn, S. Oh, J.-U. Bae, S.-J. Choi, D. H. Kim, D. M. Kim, *IEEE Electron Device Lett.* **2013**, *34*, 1524.
- [32] C. Leroux, J. Mitard, G. Ghibaudo, X. Garros, G. Reimbold, B. Guillaumot, F. Martin, *Int. Electron Devices Meet. – IEDM Tech. Dig.* **2004**, 737.
- [33] S. Lee, K. Ghaffarzadeh, A. Nathan, J. Robertson, S. Jeon, C. Kim, I. Song, U.-I. Chung, *Appl. Phys. Lett.* **2011**, *98*, 203508.
- [34] K. Nomura, H. Ohta, A. Takagi, T. Kamiya, M. Hirano, H. Hosono, *Nature* **2004**, *432*, 488.
- [35] J.-K. Kim, K. Cho, T.-Y. Kim, J. Pak, J. Jang, Y. Song, Y. Kim, B. Y. Choi, S. Chung, W.-K. Hong, T. Lee, *Sci. Rep.* **2016**, *6*, 36775.
- [36] H. Liu, J. Gu, P. D. Ye, *IEEE Electron Device Lett.* **2012**, *33*, 1273.